

Impact of leakage on sound properties of 3D printed samples at normal and grazing incidence

Alexis Jamois,^{a)}  Didier Dragna,  and Marie-Annick Galland

Ecole Centrale de Lyon, Centre National de la Recherche Scientifique, Université Claude Bernard Lyon 1, Institut National des Sciences Appliquées Lyon, LMFA, Unité Mixte de Recherche 5509, 69130, Ecully, France

ABSTRACT:

The impact of leakage on sound properties of open porosity 3D printed samples with a periodic microstructure is investigated at normal and grazing incidence. For that, direct numerical simulations (DNS) accounting for leakage are performed. In addition, an extension of the model proposed by Cummings [(1991). *J. Sound Vib.* **151**, 63–75] is developed to predict the surface impedance of a sample surrounded by an air space at normal impedance accounting for dissipation in the leak. Experiments in a Kundt tube are performed for three series of 3D printed samples with different external diameter. Overall, leakage is responsible for a shift of the absorption peak toward higher frequencies and to an increase in its amplitude. Comparison of the measurements with the DNS and the extended Cummings model shows that both approaches predict satisfactorily the impact of leakage on the absorption coefficient. In addition, a duct wall configuration is studied for three geometries of 3D printed samples. DNS results reveal that the impact of leakage on transmission loss varies significantly depending on the 3D printed sample unit cell. Finally, discrepancies between the measured and predicted transmission loss are shown to be attributable to leakage for two of the three geometries. © 2025 Acoustical Society of America. <https://doi.org/10.1121/10.0037074>

(Received 6 March 2025; revised 4 June 2025; accepted 12 June 2025; published online 3 July 2025)

[Editor: Michael R. Haberman]

Pages: 75–83

I. INTRODUCTION

Additive manufacturing allows for the realization of shapes and devices that were previously impossible to obtain with classic machining. It has been intensively used for creating acoustic absorbers based on quarter-wavelength coiling resonators (Almeida *et al.*, 2021; Wang *et al.*, 2018), Helmholtz resonators (Guo *et al.*, 2021; Duan *et al.*, 2020; Cavalieri *et al.*, 2019; Al Jahdali and Wu, 2018), labyrinthine channels in microporous skeletons (Zieliński *et al.*, 2024), or open porosity devices (Boulvert *et al.*, 2019; Zieliński *et al.*, 2020a, 2020b; Jamois *et al.*, 2025). Acoustic performance is generally assessed at normal incidence using a Kundt tube in which the sample is inserted. It can also be evaluated at grazing incidence for mufflers or for aeronautical applications, for instance. For that, the sample is mounted at the surface of a duct (Boulvert *et al.*, 2022a, 2022b; Oh and Jeon, 2022) and often held in place by a sample holder. Those techniques are widely used and robust for characterizing foam and fibrous materials. Because these materials are compressible, the size of the samples can be made slightly larger than the allowed space in the tube or in the sample holder while being easily mountable, preventing from any leakage around the sample. However, as 3D printed samples can hardly be compressed in comparison with the previously cited materials, it is necessary to maintain a mechanical slack to adapt the sample to the bench. In addition, the realization uncertainties of these 3D printing techniques (Fusaro *et al.*, 2023) can increase the difficulty to

match accurately the dimensions of the sample with those of the testing bench. Moreover, the resonant geometries realized with 3D printing techniques are very sensitive to these defects. Strategies have been proposed to minimize the slack, such as machining the sample with a lathe (Zieliński *et al.*, 2022) or using a laser cutting machine. However, a small leakage inevitably remains. Different techniques are then employed to fill the slack, such as using acoustic grease around the sample, wrapping the sample in duct tape, including an impervious coat in the printed sample, or covering the sample with a thin layer of a highly resistive porous material.

While the negative effects of leakage on acoustic measurements are well known, few studies have sought to quantify its impact. Cummings (1991) proposed an analytical model for the equivalent surface impedance of a porous sample surrounded by a lossless air gap in a Kundt tube. This analytical model applied to foams shows a slight shift in the absorption coefficient toward higher frequencies due to leakage. Kino and Ueno (2007) investigated impedance tube measurements of undersized and oversized samples of fibrous materials and concluded that the elastic behavior due to the strain of an oversized sample had a more detrimental effect on the measurement than leakage. Lee *et al.* (2013) studied the effect of holes in Helmholtz and quarter-wavelength resonators mounted on a duct wall using both experiments and analytical models. Their findings reveal that leakage tends to shift the transmission loss (TL) peak to higher frequencies while reducing its amplitude.

This work aims to investigate the effect of leakage on the acoustic performance measurement of open porosity 3D

^{a)}Email: alexis.jamois@ec-lyon.fr

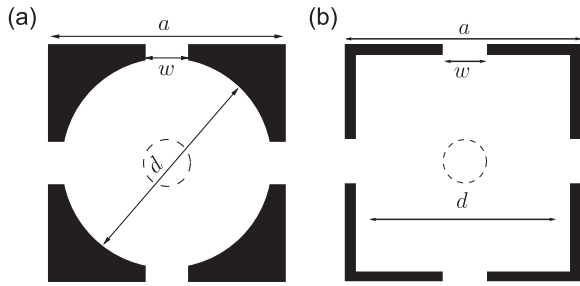


FIG. 1. Sketch of the two unit cells studied in this work with a (a) spherical or (b) cubic cavity.

printed samples at normal and grazing incidence. For that, experiments in a Kundt tube and in a duct bench are performed and results are compared to direct numerical simulations (DNS) and analytical models. In particular, for Kundt tube configurations, an extension of the Cummings model accounting for dissipation in the leak is proposed.

The paper is organized as follows. In Sec. II, the geometry and the realization characteristics of the 3D printed samples are presented. Section III describes the analytical and numerical approaches to predict the effect of leakage in an impedance tube. In Sec. IV, the results at normal incidence are presented. Section V is devoted to results at grazing incidence. Concluding remarks are given in Sec. VI.

II. DESCRIPTION OF THE GEOMETRIES

Three geometries, based on the geometry considered in the round robin study of Zieliński *et al.* (2020b), are examined. They consist of a periodic microstructure of cavities (spherical or cubic) linked to each other in the three directions of space by small cylindrical channels.

TABLE I. Characteristic dimensions of the unit cell for the three geometries.

Designation	Cavity	a (mm)	d (mm)	w (mm)
OPC	Spherical	5	4.5	2
OPCL	Spherical	9	8	1.5
Cubic	Cubic	9	8	1.5

A sketch of the unit cells is presented in Fig. 1. The design dimensions of the unit cells for the three geometries are given in Table I. The first two ones denoted OPC (one pore cell) and OPCL (one pore cell large) have a spherical cavity and the third one denoted cubic has a cubic cavity. As indicated in Jamois *et al.* (2025), these geometries are highly tortuous and, as a consequence, are very sensitive to leakages.

Only the OPCL geometry is considered for Kundt tube measurements in Sec. IV. The Kundt tube is circular with a diameter $d_K = 29$ mm. For grazing incidence in Sec. V, a sample of each geometry is printed with a length L_t of 150 mm and a width l_t of 66 mm. For both the Kundt tube and the duct bench, the thickness of the samples is 31.5 mm for the cubic and OPCL geometry and 32.5 mm for the OPC geometry. This leads to an odd number of half cells in the thickness of the material. The faces at the two ends of the material are thus different. The impact of these two different surfaces on the acoustic properties of the samples is studied in Jamois *et al.* (2025). This present work focuses on the sample face showing open cavities. The samples are realized with the stereolithography technique using a Form2 from Formlabs with their Clear-04 resin and a printing resolution of 0.025 mm. A picture of the samples is shown in Fig. 2. The study conditions are the same as described in Jamois *et al.* (2025).

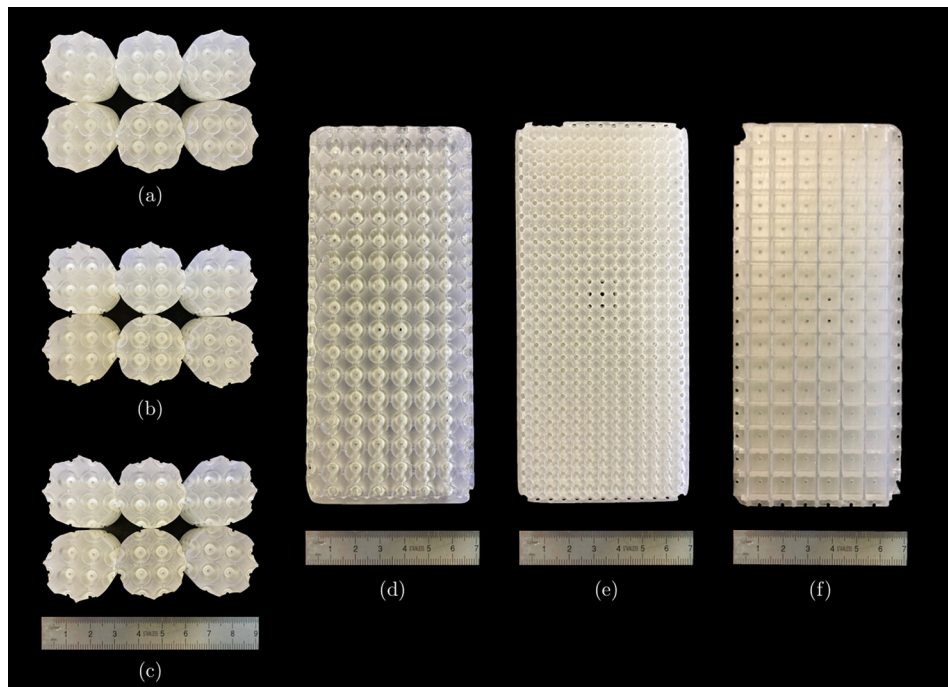


FIG. 2. Picture of the three OPCL sample series for the Kundt tube [series A in (a), series B in (b), and series C in (c)] and of the (d) OPCL, (e) OPC, and (f) cubic samples for duct bench.

III. MODELING OF THE SAMPLE AND OF LEAKAGE AT NORMAL INCIDENCE

A. Analytical model

1. Formulation

In the case of an impedance tube, Cummings (1991) has proposed an analytical model to predict the effect of leakage on the acoustic properties of a porous sample. Although the model was originally developed for an anisotropic porous material, we focus here solely on an isotropic material. The leakage and the sample have a uniform cross section along the tube, denoted by S_1 and S_2 , respectively. The surface ratio $\phi_l = S_1/S_2$ is introduced. The porous sample is modeled by an equivalent fluid with dynamic density ρ_c and wavenumber k_c . The density and wavenumber of air in the leakage are denoted ρ_a and k_a , respectively. We denote also by ρ_0 and $k_0 = \omega/c_0$ the density and wavenumber in lossless air with $\omega = 2\pi f$ the angular frequency and c_0 the sound speed in air. The wavenumber of the fundamental mode propagating in the Kundt tube k_{eff} can then be determined, which allows the effective properties of the sample to be computed.

Using the convention $e^{i\omega t}$, the surface impedance of the porous sample with an air gap is given by the following:

$$Z_s = \frac{\omega \rho_c}{k_{\text{eff}}} \frac{\coth(ik_{\text{eff}}L)}{1 + \epsilon_l(\rho_c/\rho_a - 1)} \quad (1)$$

with $\epsilon_l = \phi_l/(1 + \phi_l)$ and

$$k_{\text{eff}} = k_c \left[\frac{1 + \phi_l k_a^2 \rho_c / (k_c^2 \rho_a)}{1 + \phi_l \rho_c / \rho_a} \right]^{1/2} \quad (2)$$

Cummings considers the air as a non-dissipative fluid, i.e., $k_a = k_0$ and $\rho_a = \rho_0$. Actually, as the thickness of the air gap around the sample is expected to be small (typically on the order of the viscous and thermal boundary layer thicknesses), dissipative processes can be important. We propose an extended model that accounts for thermoviscous losses in the leak. For that, we use the slit model to determine the dynamic density and compressibility of the air as follows:

$$\rho_a = \rho_0 \left[1 - \frac{\tanh(\sqrt{i}\beta)}{\sqrt{i}\beta} \right]^{-1} \quad (3)$$

$$K_a = \rho_0 c_0^2 \left[1 + (\gamma - 1) \frac{\tanh(\sqrt{i\text{Pr}}\beta)}{\sqrt{i\text{Pr}}\beta} \right]^{-1}, \quad (4)$$

and $k_a = \omega \sqrt{\rho_a/K_a}$. Pr is the Prandtl number set to 0.72 for air. The parameter β is given by $\beta = a_c \sqrt{\omega \rho_0 / \eta}$, with a_c the half-width of the slit and η the dynamic viscosity. We can estimate a_c by considering that the air gap corresponds to an annulus of constant thickness $e = 2a_c$ around the sample [see Fig. 3(a)]. The cross-sections of the air gap and of the porous sample are thus equal to $S_1 = \pi[d_K^2 - (d_K - 4a_c)^2]/4$ and $S_2 = \pi(d_K - 4a_c)^2/4$. We deduce the following:

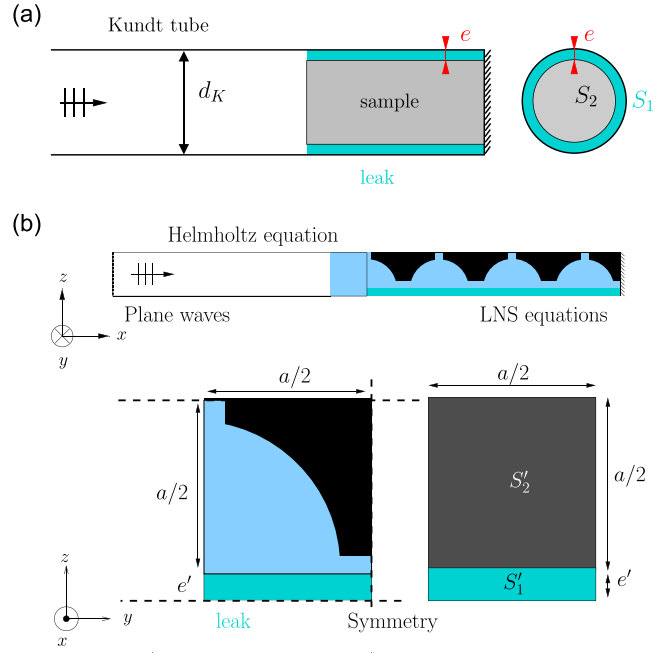


FIG. 3. Sketch of the leakage in the experimental impedance tube (a) and the chosen configuration in the DNS (b).

$$a_c = \frac{d_K}{4} \left(1 - \frac{1}{\sqrt{1 + \phi_l}} \right) \approx \frac{d_K \phi_l}{8} \quad (5)$$

Note that the leak impact in the extended Cummings model depends on the ratio of the leak cross section to that of the sample and also on the ratio of a characteristic size of the leak to that of the viscous and thermal boundary layer thicknesses through the parameter β . In contrast, the original Cummings model only accounts for the surface ratio ϕ_l . Furthermore, when the characteristic size of the leak is significantly larger than the viscous and thermal boundary layer thicknesses ($\beta \gg 1$), $\rho_a \approx \rho_0$ and $K_a \approx \rho_0 c_0^2$, reducing the extended Cummings model to its original form.

2. Equivalent fluid model

For application of the Cummings model, the sample has to be represented as an equivalent fluid. For materials with a periodic microstructure, such as those considered in this work, the parameters of the Johnson-Champoux-Allard-Prède-Lafarge model can be determined from the unit cell. This methodology, referred to as hybrid multiscale calculation, requires to solve the Laplace, Stokes and Poisson problems in the unit cell. To do so, we use the finite-element commercial software COMSOL. The absorption coefficient calculated with this methodology has been compared successfully to that obtained by DNS for the three geometries considered in this study. More details can be found in [Jamois et al. \(2025\)](#).

B. DNS

DNS consist of directly solving the mechanics equations in the material to deduce its acoustic properties. Due to

the realization technique, the skeleton can be considered as rigid and without any porosity. As a consequence, it is sufficient to solve in the pores of the material the full set of linearized Navier-Stokes (LNS) equations, that accounts for thermoviscous effects.

Denoting by p , T , and \mathbf{v} , the acoustic pressure, temperature, and velocity, the LNS equation of motion, the mass conservation equation, and the heat conduction equation read as follows:

$$i\omega\rho_0\mathbf{v} = -\nabla p + \eta\left(\nabla^2\mathbf{v} + \frac{1}{3}\nabla(\nabla\cdot\mathbf{v})\right) \quad (6)$$

$$i\omega\left(\frac{p}{\rho_0} - \frac{T}{T_0}\right) + \nabla\cdot\mathbf{v} = 0 \quad (7)$$

$$i\omega\rho_0c_pT = \kappa\nabla^2T + i\omega p, \quad (8)$$

where p_0 and T_0 are the ambient values of air pressure and temperature, c_p is its specific heat capacity at constant pressure, and κ is its thermal conductivity. At the fluid/structure interface, a no-slip condition $\mathbf{v} = \mathbf{0}$ and an isothermal condition $T = 0$ are applied.

DNS have a high computational cost due to the necessity of meshing the acoustic boundary layers to accurately account for thermoviscous losses. Due to the periodic microstructure and to the symmetries of the unit cell, only a single stack of cells along the impedance tube direction needs to be considered, with meshing required for just a quarter of a cell. This significantly reduces the computational cost of the DNS. To model the leakage with DNS, a thin air-filled volume of thickness e' , in which the LNS equations are solved as well, is added adjacent to the pores. Finally, the Helmholtz equation is solved instead of LNS equations at a sufficient distance from the sample, where thermoviscous losses become negligible. The resulting impedance tube configuration in the DNS is illustrated in Fig. 3(b). The quarter of a cell can be observed in the acoustic propagation plane with the leak near the spherical cavities. A cross section of the tube is also shown, highlighting the surfaces corresponding to the sample and to the leak.

Simulations have been performed using the finite-element commercial software COMSOL without leakage and with leakage for five leak thicknesses e' reported in Table II. The finer the leak, the greater the computational cost in terms of time and memory, as mesh continuity is required. Thus, the mesh contains about 60 000 elements for the configuration without leak and above 250 000 elements for the smallest leak thickness. For the case without leak,

the computation takes 6.5 h on six compute nodes of 16 cores for 300 frequency steps. With the smallest leak thickness, simulations are run on six compute nodes of 32 cores and demand over 300 GB of memory.

Since the full sample geometry is not considered in the DNS, it is not possible to keep the same surface ratio ϕ_l and same leak thickness as in the actual sample. Indeed, one has $\phi_l = S_1/S_2 \approx 4e/d_K$ from Eq. (5) and $\phi_l = S'_1/S'_2 = 2e'/a$ in DNS. For comparison with the other models and measurements, we choose to keep the same value of ϕ_l , which is the most representative parameter for characterizing the problem. As a consequence, the leak thickness in the DNS is slightly underestimated, as indicated in Table II.

IV. RESULTS AT NORMAL INCIDENCE

This section focuses on normal incidence for the OPCL geometry only. A comparison of the three models accounting for leakage introduced in Sec. III is presented, along with a parametric study on the impact of leakage. Then, the acoustic absorption coefficients measured for 3D printed samples with three different external diameters are reported and are compared with the predicted absorption coefficients, both with and without leakage.

A. Numerical study

Figure 4(a) displays the absorption coefficient of the OPCL sample with and without leakage using the design dimensions reported in Table I. The reference absorption coefficient without leakage shows a single peak centered at 1200 Hz with a maximum value of 0.83. The absorption coefficients with leakage are obtained for a surface ratio $\phi_l = 0.022$ with the DNS, the Cummings model, and the extended Cummings model. The DNS shows that the leakage is responsible for a shift of the absorption peak toward higher frequencies with a maximum around 1350 Hz. In addition, the peak width significantly increases. Thus, the peak width at half-height is 430 Hz without leakage and 600 Hz with leakage. Finally, the peak amplitude also increases with a maximal value close to one with leakage. The Cummings model gives a correct prediction of the peak frequency but largely underestimates the peak amplitude. The extended Cummings model, which accounts for the dissipation in the leak, offers better agreement with DNS, especially for the peak amplitude, but yields a narrower peak.

Figure 4(b) presents the impact of the leakage on the absorption coefficient, focusing on the amplitude and frequency of the first absorption peak denoted by α_{\max} and f_{\max} , respectively. The reference DNS results show that a leakage with a surface ratio as small as 0.2% leads to a significant increase in the absorption coefficient. The maximum of absorption coefficient remains close to one as ϕ_l increases, but starts decreasing for $\phi_l > 2\%$. The frequency of the first absorption peak first slightly decreases for $\phi_l < 1\%$ and then significantly increases with ϕ_l . Unlike DNS, the Cummings model predicts a linear decrease in α_{\max} , considerably underestimating the maximum absorption coefficient. It also

TABLE II. Correspondence between the leak thickness e' used in DNS, the surface ratio ϕ_l , and the equivalent leak thickness around the Kundt tube sample e .

e' (mm)	0.01	0.05	0.075	0.1	0.2
ϕ_l	0.0022	0.0111	0.0167	0.022	0.044
e (mm)	0.016	0.080	0.12	0.16	0.32

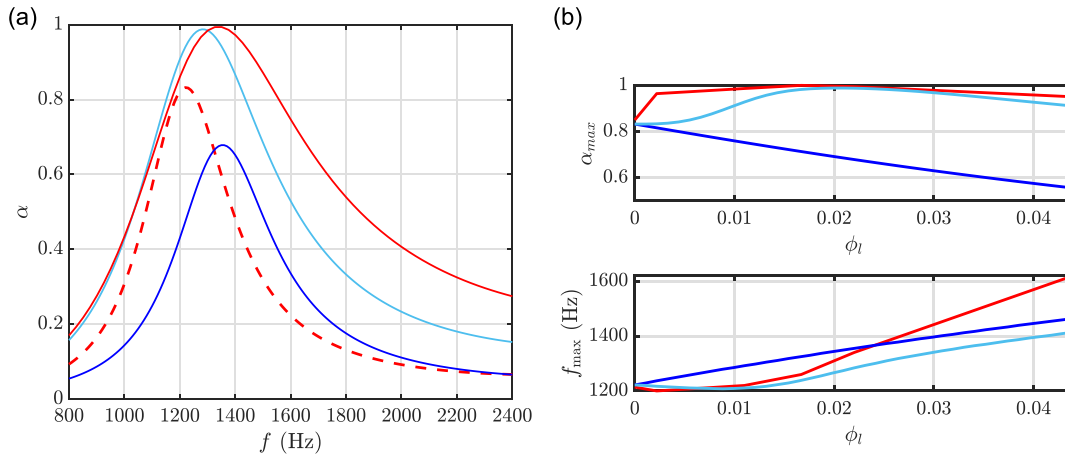


FIG. 4. (a) Absorption coefficient for an OPCL sample with a leakage surface ratio $\phi_l=0.022$ obtained with DNS (red solid line), the Cummings model (blue solid line), and the extended Cummings model (cyan solid line). The reference absorption coefficient without leakage is plotted in the red dashed line. (b) Amplitude and frequency of the absorption coefficient peak as a function of the surface ratio ϕ_l for the three models accounting for the leak.

shows a continuous increase in the frequency of the first absorption peak with ϕ_l . Finally, the extended Cummings model, which accounts for dissipation in the leakage, provides a good match with DNS. In particular, it predicts the same evolution of α_{max} and f_{max} with ϕ_l as observed in DNS. However, for small values of ϕ_l , α_{max} increases more gradually than in DNS. Additionally, the increase in the peak frequency for $\phi_l > 2\%$ is similar to that of the Cummings model, evolving more slowly than in DNS.

B. Description of the experiments

Three processes are considered to make the samples fit in the Kundt tube. We produced for each of these processes a series of six OPCL samples to reduce the uncertainties due to additive manufacturing. For the samples in series A, the default calibration of the 3D printer was used, resulting in an external diameter larger than that of the Kundt tube. The samples were sanded by hand, which led to a loss of cylindricity. For the series B, the 3D printer was carefully calibrated so that the external diameter of the samples almost matches the Kundt tube diameter. Finally, the samples in the

series C were intentionally printed with a diameter larger than that of the Kundt tube and were subsequently machined using a lathe to achieve a tight fit in the Kundt tube.

Figure 5 presents the average external diameter of the samples for each series determined using a calliper. The samples in the series A have on average the smallest external diameter, equal to 28.27 mm. The average diameters for the two other series are closer to that of the Kundt tube, with 28.81 mm for series B and 28.91 mm for series C. Lathe machining offers the closest fit to the Kundt tube diameter and also the least dispersion.

Note that the characteristic dimensions of 3D printed samples may deviate from the design values. In addition, as the printing procedure is different for each series, the characteristic dimensions of the samples may also differ from one series to another. In order to have accurate inputs for the models, we measured the characteristic dimensions (sphere and channel diameters) of the eight cells visible on both bases of the cylindrical sample for all samples, using a Mitutoyo PJ-A3000 profile projector (see [Jamois et al., 2023](#) for details). The average values per series were then used to generate the geometry in the DNS and also to identify the parameters of the Johnson-Champoux-Allard-Pride-Lafarge model in the hybrid multiscale calculation. They are reported in Table III.

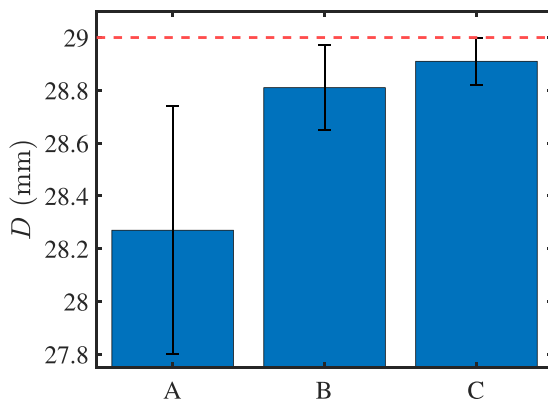


FIG. 5. Average external diameter of the samples for each series. The error bar indicates the minimum and maximum external diameter. The dashed line corresponds to the Kundt tube diameter.

C. Comparison with experimental results

Figure 6 shows the absorption coefficient for each series obtained by averaging those measured for the six samples.

TABLE III. Average characteristic dimensions of the unit cells for the three sample series. The values are obtained from the six samples of each series.

Series	d (mm)	w (mm)	e (mm)	ϕ_l
A	8.14	1.34	0.36	0.052
B	8.01	1.31	0.10	0.013
C	7.99	1.18	0.05	0.007

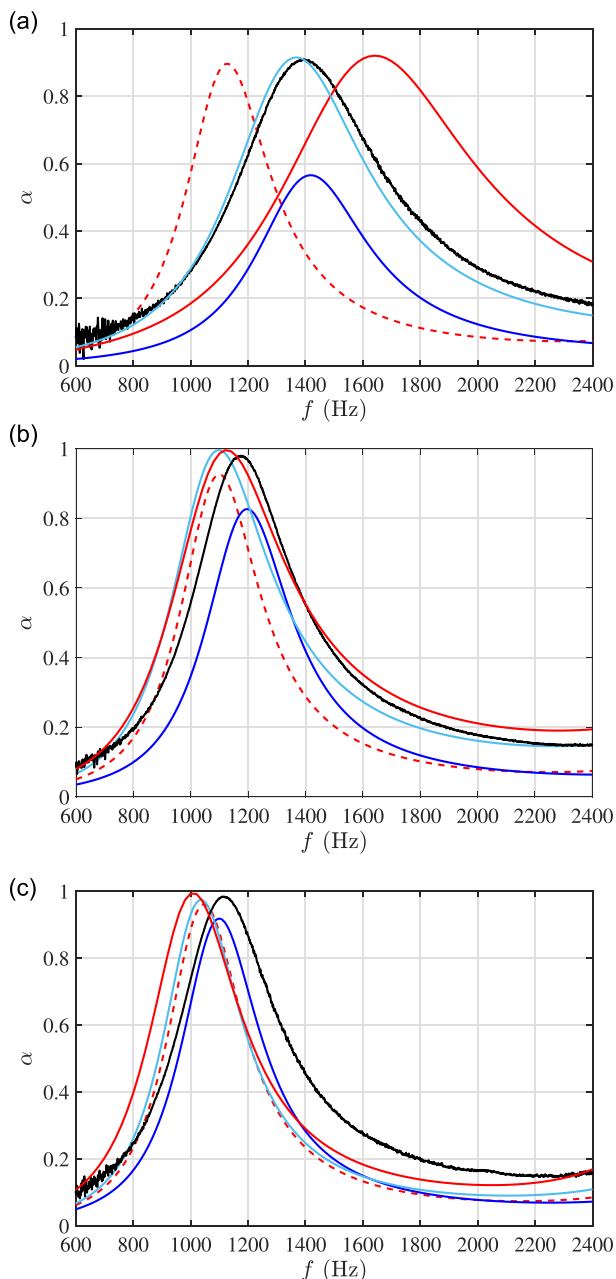


FIG. 6. Measured absorption coefficient averaged over the six samples per series (black solid line) and obtained from DNS (red solid line), the Cummings model (blue solid line), and the extended Cummings model (cyan solid line) for series A in (a), series B in (b), and series C in (c). The absorption coefficient without leakage obtained with DNS is plotted in the red dashed line.

The absorption coefficients calculated using DNS with and without leakage, the Cummings model, and the extended Cummings model are also plotted. The values of e and ϕ_l used in the models are indicated for each series in Table III. Note that, for comparison with the models, the samples were introduced in the Kundt tube as is, without duct tape or any process to reduce leakage. First, let us compare the experimental results and the DNS without leakage. For the series A in Fig. 6(a), the measured absorption peak occurs at a frequency more than 250 Hz higher than predicted by DNS

without leakage, while its amplitude remains quite similar. For the series B and C in Figs. 6(b) and 6(c), the difference in the peak frequency is lower (around 100 Hz). The peak amplitude is in better agreement in the series C than in the series B. These results are coherent with the reduction of leakage in the series B and C compared to series A.

Let us now examine the models with leakage. For the series A, all three models capture the shift of the absorption peak toward higher frequencies, but this effect is exaggerated in the DNS. The difference in peak frequency between the measurements and the DNS has yet to be explained. The peak amplitude observed in the experiments aligns closely with both the DNS and the extended Cummings model, whereas the Cummings model tends to underestimate it. Overall, the extended Cummings model exhibits excellent agreement with the measurements. For the series B, both the DNS and the extended Cummings model closely match the measurements. However, the shift in the frequency peak is more pronounced in the experiments than in the models. Additionally, the Cummings model once again underestimates the peak amplitude. For the series C, as the leak thickness is small, the three models give close results and agree well with the measurements. One can observe that the DNS and the extended Cummings model predict a shift of the frequency peak toward lower frequencies. This trend is not observed in the measurements.

V. RESULTS AT GRAZING INCIDENCE

A. Description of the experiments

This section investigates the impact of leakage on TL for a 3D printed liner at grazing incidence. To do so, we use the MATISSE duct at LMFA with a cross section of 66 mm \times 66 mm (see Sellen *et al.*, 2006 for details). The duct cut-off frequency is approximately 2.5 kHz, meaning that only plane waves propagate below this frequency. Two pairs of microphones are placed before and after the liner to determine the TL [see Fig. 7(a)].

3D printed samples based on the three geometries introduced in Sec. II were produced. They were mounted in a sample holder placed at the surface of the duct. A particular attention was paid to the design of the sample holder to reduce leakage. At its interface with the duct, the holder features a 3 mm flange on which the sample rests to minimize potential leaks along the sample edges. The sample was then inserted by force in the holder. Finally, the holder cover was pushed toward the sample using a screw-tightening system. Despite the precautions taken, leakage can still occur at the sides of the sample or at its back. Unlike in an impedance tube, estimating the air space is not straightforward.

B. Description of the DNS

There is no analytical model in the literature to quantify the effect of leakage around the samples on TL for duct wall configurations. Consequently, we rely solely on DNS to predict the TL of the samples, both with and without leakage. As for normal incidence, the full sample geometry is not

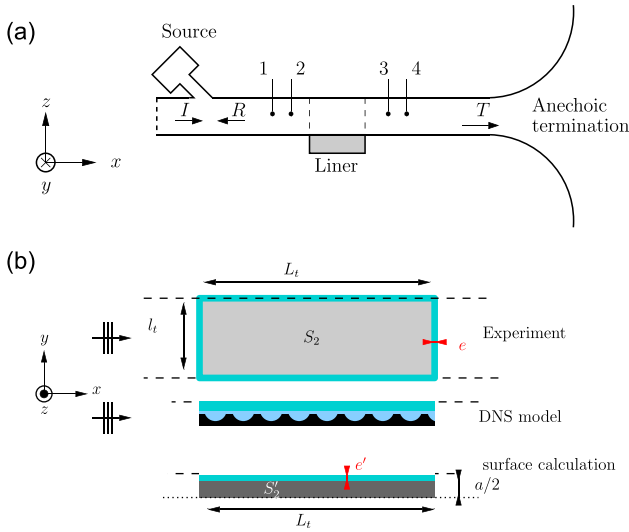


FIG. 7. (a) Sketch of the MATISSE duct for TL measurement. (b) Sketch illustrating the equivalent leak thickness in the DNS.

considered to reduce the computational cost. Instead, due to the periodic microstructure, a single layer of cells along the duct axis is modeled; and due to symmetries, only half of a cell is meshed. A leakage of thickness e' is introduced on the cavity side of the cells. To choose a relevant value for e' , we assume that the air space surrounding the actual sample has a constant thickness e , as illustrated in Fig. 7(b). We choose to keep the same value of ϕ_l , i.e., the ratio of the air gap surface to the sample surface, between the experiments and the model. Due to meshing constraint, we are limited to a minimum leak thickness $e' = 0.1$ mm, which results in $\phi_l = 0.022$, to ensure proper account of the dissipation in this leakage. This value of ϕ_l corresponds to a leak thickness $e = 0.5$ mm all around the actual sample, which is of the correct order of magnitude but may be slightly overestimated. Note that actually, the leak thickness is not uniform around the sample, and the mechanisms at play are probably more complicated than those modeled. DNS for the duct case are extremely computationally demanding. Each simulation involves over one million elements and is run on six compute nodes of 32 cores, requiring more than 1TB of memory.

C. Comparison

TL is presented for the three geometries in Fig. 8. For the OPCL sample in Fig. 8(a), the TL predicted by DNS without leakage shows a single peak centered at 1250 Hz with an amplitude of 26 dB. In the experiments, the peak is observed at the same frequency but is much more rounded and reaches only 8 dB. Taking into account for leakage, the DNS provide a close match with the experiments. In this case, the reduction in TL is satisfactorily explained by leakage. For the OPC sample in Fig. 8(b), the TL predicted by DNS has two peaks close to 1800 Hz and a third peak at 2300 Hz. While the experiments are overall in good agreement with the DNS, the peak at 1900 Hz is not observed in

the measured TL. The leakage in the DNS tends to reduce the TL and smooth its evolution with frequency. Even if the impact of leakage is overestimated in the DNS, it appears to account for the suppression of the peak at 1900 Hz in the experiments. Finally, the TL given by DNS for the cubic geometry in Fig. 8(c) presents a single peak centered at 1000 Hz and with amplitude of 18 dB. The measured TL is very similar, but the peak amplitude reaches almost 45 dB. Taking into account for leakage in the DNS results in a slight increase in the peak amplitude, reaching up to 20 dB. However, it does not reproduce the significantly higher peak amplitude observed in the experiments. Additional simulations (presented in the Appendix) indicate that increasing the leakage thickness shifts the TL peak toward higher frequencies but does not lead to a further increase in peak amplitude. For this configuration, leakage does not seem to be the primary factor responsible for the discrepancies between numerical simulations and measurements. The differences in peak amplitude remain unexplained.

VI. CONCLUSION

This study has investigated the impact of leakage on the acoustic property measurements of 3D printed samples with periodic microstructure and open porosity. To this end, both DNS and analytical models were employed. In particular, an

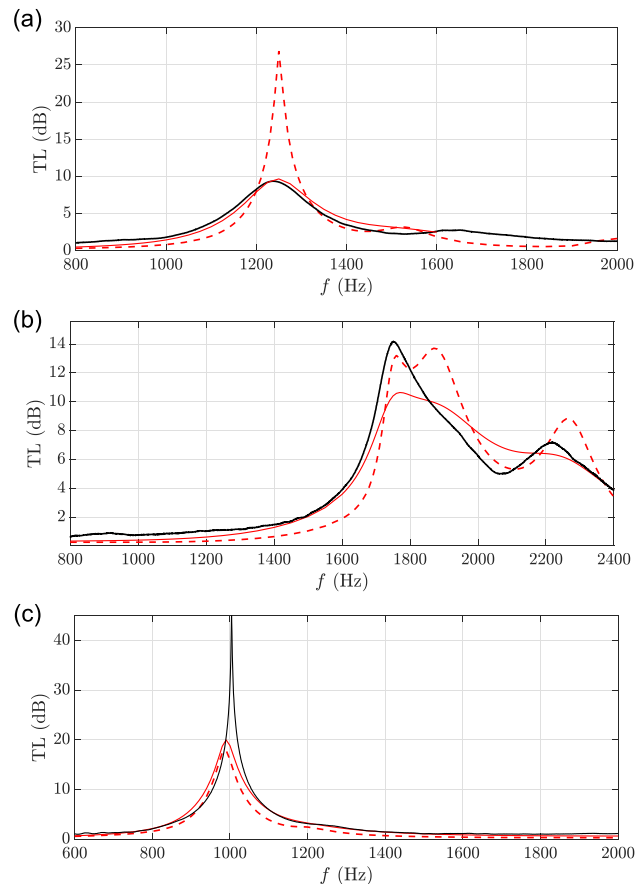


FIG. 8. TL for (a) OPCL, (b) OPC, and (c) cubic samples obtained with experiments (black solid line) and determined by DNS (red dashed line) without leak and (red solid line) with a leak with $\phi_l = 0.022$.

extension of the Cummings model was developed to determine the surface impedance of the sample in a Kundt tube, incorporating thermoviscous losses in the air leak. At normal incidence, a parametric study for a specific unit cell geometry showed that leakage leads to an increase in the absorption coefficient when the size of the leakage is small compared to that of the sample and then to a reduction when the size of the leakage is sufficiently large. Overall, the peak frequency tends to increase with the leak size. Experiments were then conducted on 3D printed samples in a Kundt tube using three procedures to ensure sealing, resulting in different external diameters. Both the extended Cummings model and the DNS were able to explain the impact of leakage on the measured absorption coefficient. Finally, the study focused on the grazing incidence case. Three samples with different unit cells were mounted in the wall of a duct. DNS showed that the leakage impact is very dependent on the sample considered: it can lead to a decrease or an increase in the TL, or even modify the global acoustic behavior. Comparison with measurements showed that leakage could explain the difference between the measured and the predicted TL for two of the three samples.

ACKNOWLEDGMENTS

This work was supported by the LABEX CeLyA (ANR-10-LABX-0060) of Université de Lyon, within the program “Investissements d’Avenir” (ANR-16-IDEX-0005) operated by the French National Research Agency. It was granted access to the HPC resources of PMCS2I (Pôle de Modélisation et de Calcul en Sciences de l’Ingénieur et de l’Information) of Ecole Centrale de Lyon. The authors would like to express their gratitude to Jean-Charles Vingiano and Bertrand Houx for their help and their precious advice on additive manufacturing; Edouard Salze and Emanuele Sarpero are also acknowledged for assistance.

AUTHOR DECLARATIONS

Conflict of Interest

The authors have no conflicts to disclose.

DATA AVAILABILITY

Data available on request from the authors.

APPENDIX

In this appendix, additional results are presented regarding the effect of leakage thickness for the duct wall configuration (see Sec. VC). As a complement to Fig. 8, Fig. 9 shows the TL computed using DNS for several values of ϕ_l and for the three material geometries. For the OPCL geometry in Fig. 9(a), we again find that leakage significantly reduces the peak amplitude. Moreover, increasing ϕ_l leads to a shift of the peak toward higher frequencies, while the peak amplitude remains nearly constant, ranging

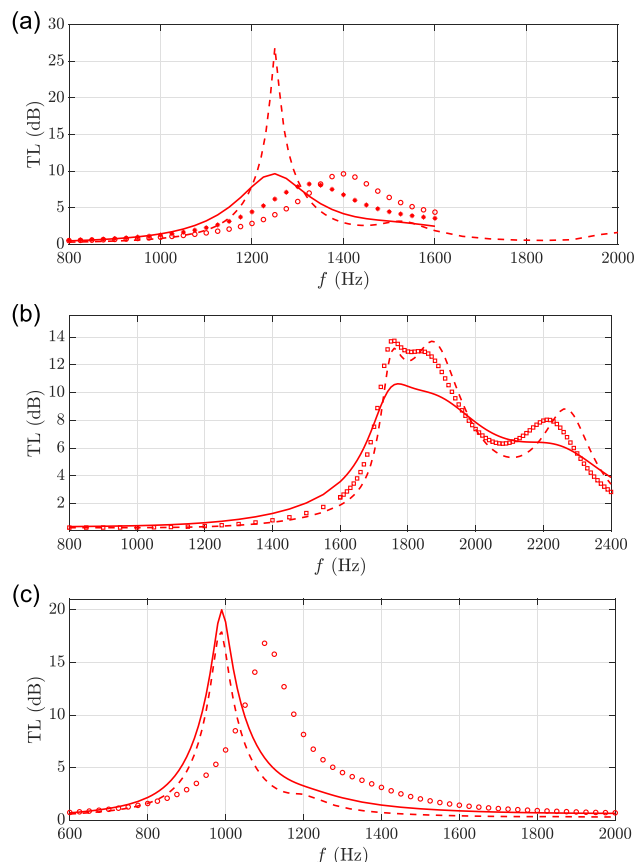


FIG. 9. TL for (a) OPCL, (b) OPC, and (c) cubic samples determined by DNS (red dashed line) without leak and with a leak using $\phi_l=0.011$ (red squares), $\phi_l=0.022$ (red solid line), $\phi_l=0.033$ (red stars), and $\phi_l=0.044$ (red circles).

between 8 and 10 dB. For the OPC geometry in Fig. 9(b), we observe that for a thinner leak ($\phi_l=0.011$) than that considered in Fig. 8(b) the third peak at 2200 Hz remains noticeable, while the second peak at 1900 Hz is already smoothed out. Thus, the TL computed with $\phi_l=0.011$ shows better overall agreement with the measurements than that obtained with $\phi_l=0.022$. Finally, for the cubic geometry in Fig. 9(c), as for the OPCL geometry, the TL peak is shifted toward higher frequencies by increasing ϕ_l , with only minor changes in amplitude compared to the configuration without leakage.

Almeida, G. D. N., Vergara, E. F., Barbosa, L. R., and Brum, R. (2021). “Low-frequency sound absorption of a metamaterial with symmetrical-coiled-up spaces,” *Appl. Acoust.* **172**, 107593.
 Al Jahdali, R., and Wu, Y. (2018). “Coupled resonators for sound trapping and absorption,” *Sci. Rep.* **8**(1), 13855–13858.
 Boulvert, J., Gabard, G., Romero-García, V., and Groby, J.-P. (2022a). “Compact resonant systems for perfect and broadband sound absorption in wide waveguides in transmission problems,” *Sci. Rep.* **12**, 10013.
 Boulvert, J., Humbert, T., Romero-García, V., Gabard, G., Fotsing, E. R., Ross, A., Mardjono, J., and Groby, J.-P. (2022b). “Perfect, broadband, and sub-wavelength absorption with asymmetric absorbers: Realization for duct acoustics with 3D printed porous resonators,” *J. Sound Vib.* **523**, 116687.
 Boulvert, J., Cavalieri, T., Costa-Baptista, J., Schwan, L., Romero-García, V., Gabard, G., Fotsing, E. R., Ross, A., Mardjono, J., and Groby, J.-P.

- (2019). “Optimally graded porous material for broadband perfect absorption of sound,” *J. Appl. Phys.* **126**(17), 175101–175115.
- Cavalieri, T., Cebrecos, A., Groby, J.-P., Chaufour, C., and Romero-García, V. (2019). “Three-dimensional multiresonant lossy sonic crystal for broadband acoustic attenuation: Application to train noise reduction,” *Appl. Acoust.* **146**, 1–8.
- Cummings, A. (1991). “Impedance tube measurements on porous media: The effects of air-gaps around the sample,” *J. Sound Vib.* **151**(1), 63–75.
- Duan, M., Yu, C., Xu, Z., Xin, F., and Lu, T. J. (2020). “Acoustic impedance regulation of Helmholtz resonators for perfect sound absorption via roughened embedded necks,” *Appl. Phys. Lett.* **117**(15), 151904.
- Fusaro, G., Barbaresi, L., Cingolani, M., Garai, M., Ida, E., Prato, A., and Schiavi, A. (2023). “Investigation of the impact of additive manufacturing techniques on the acoustic performance of a coiled-up resonator,” *J. Acoust. Soc. Am.* **153**(5), 2921–2931.
- Guo, J., Fang, Y., Jiang, Z., and Zhang, X. (2021). “An investigation on noise attenuation by acoustic liner constructed by Helmholtz resonators with extended necks,” *J. Acoust. Soc. Am.* **149**(1), 70–81.
- Jamois, A., Dragna, D., and Galland, M.-A. (2023). “Impact of manufacturing uncertainties on the acoustic properties of 3D printed materials” in *29th International Congress on Sound and Vibration [ICSV29]*, International Institute of Acoustics and Vibration IIAV, Prague, Czech Republic.
- Jamois, A., Dragna, D., Zieliński, T. G., and Galland, M.-A. (2025). “Acoustic absorption of 3D printed samples at normal incidence and as a duct liner,” *Acta Acust.* **9**, 1–18.
- Kino, N., and Ueno, T. (2007). “Investigation of sample size effects in impedance tube measurements,” *Appl. Acoust.* **68**(11), 1485–1493.
- Lee, I., Jeon, K., and Park, J. (2013). “The effect of leakage on the acoustic performance of reactive silencers,” *Appl. Acoust.* **74**(4), 479–484.
- Oh, T. S., and Jeon, W. (2022). “Acoustic metaliners for sound insulation in a duct with little flow resistance,” *Appl. Phys. Lett.* **120**, 044103.
- Sellen, N., Cuesta, M., and Galland, M.-A. (2006). “Noise reduction in a flow duct: Implementation of a hybrid passive/active solution,” *J. Sound Vib.* **297**(3), 492–511.
- Wang, Y., Zhao, H., Yang, H., Zhong, J., Zhao, D., Lu, Z., and Wen, J. (2018). “A tunable sound-absorbing metamaterial based on coiled-up space,” *J. Appl. Phys.* **123**, 185109.
- Zieliński, T. G., Opiela, K. C., Dauchez, N., Boutin, T., Galland, M.-A., and Attenborough, K. (2024). “Extremely tortuous sound absorbers with labyrinthine channels in non-porous and microporous solid skeletons,” *Appl. Acoust.* **217**, 109816.
- Zieliński, T. G., Venegas, R., Perrot, C., Červenka, M., Chevillotte, F., and Attenborough, K. (2020a). “Benchmarks for microstructure-based modeling of sound absorbing rigid-frame porous media,” *J. Sound Vib.* **483**, 115441.
- Zieliński, T. G., Opiela, K. C., Pawowski, P., Dauchez, N., Boutin, T., Kennedy, J., Trimble, D., Rice, H., Van Damme, B., Hannema, G., Wróbel, R., Kim, S., Ghaffari Mosanenzadeh, S., Fang, N. X., Yang, J., Briere de La Hossieraye, B., Hornikx, M. C., Salze, E., Galland, M.-A., Boonen, R., Carvalho de Sousa, A., Deckers, E., Gaborit, M., and Groby, J.-P. (2020b). “Reproducibility of sound-absorbing periodic porous materials using additive manufacturing technologies: Round robin study,” *Addit. Manuf.* **36**, 101564.
- Zieliński, T. G., Dauchez, N., Boutin, T., Leturia, M., Wilkinson, A., Chevillotte, F., Bécot, F.-X., and Venegas, R. (2022). “Taking advantage of a 3D printing imperfection in the development of sound-absorbing materials,” *Appl. Acoust.* **197**, 108941.